

Controlling tilted chiral magnetic textures in Janus Nb*X*Te (*X* = Se, S) monolayers via magnetic field and strain engineering

Xiao-Bo Yu(于晓波), Dong Fan (范栋), and Chang-Wen Zhang(张昌文)
Citation: Chin. Phys. B, 2026, 35 (**3**): 037504. DOI: 10.1088/1674-1056/ae3c8a
http://cpb.iphy.ac.cn; http://iopscience.iop.org/cpb

What follows is a list of articles you may be interested in

Hall anomalies in the centrosymmetric triangular-lattice antiferromagnet $GdGa_2$

Sidi Wang(王思迪), Jiyuan Li(李纪源), Yuhao Wang(王宇豪), Keqi Xia(夏克奇), Jing Meng(孟婧), Bocheng Yu(余博丞), Yiqian Hu(胡艺骞), Zheng Li(李峥), Hui Zhang(张慧), Jingzhong Luo(罗晶中), Dongmei Jiang(蒋冬梅), Qingfeng Zhan(詹清峰), Tian Shang(商恬), and Yang Xu(徐杨)
Chin. Phys. B, 2026, 35 (**2**): 027502. DOI: 10.1088/1674-1056/ae2672

Magnetoelectric topology: The rope weaving in parameter space

Ying Zhou(周颖), Ziwen Wang(王子文), Fan Wang(王凡), Haoshen Ye(叶浩燊), and Shuai Dong(董帅)
Chin. Phys. B, 2026, 35 (**2**): 027501. DOI: 10.1088/1674-1056/ae2c6b

Deformation of magnetic skyrmion due to skyrmion-skyrmion interaction

Zhen-Qian Cui(崔振茜), Wen-Li Yang(杨文力), and Jun-Hui Zheng(郑俊辉)
Chin. Phys. B, 2025, 34 (**7**): 077502. DOI: 10.1088/1674-1056/adca20

Stability and characteristic modes of skyrmions in magnetic nanotubes

Tijjani Abdulrazak, Qizhi Cai(蔡淇智), and Guangwei Deng(邓光伟)
Chin. Phys. B, 2025, 34 (**10**): 107512. DOI: 10.1088/1674-1056/ade071

Strain-manipulated dispersion characteristics of magnonic crystals with Dzyaloshinskii-Moriya interaction and applications on spin-wave devices

Chuhan Zhou(周楚涵), Xiaotian Jiao(焦晓天), Jiaxi Xu(徐佳熙), Zhaonian Jin(金兆年), Lin Chen(陈琳), and Zhikuo Tao(陶志阔)
Chin. Phys. B, 2025, 34 (**2**): 027501. DOI: 10.1088/1674-1056/ad9892

Controlling tilted chiral magnetic textures in Janus NbXTe (X = Se, S) monolayers via magnetic field and strain engineering

Xiao-Bo Yu(于晓波), Dong Fan (范栋), and Chang-Wen Zhang(张昌文)†

School of Physics and Technology, University of Jinan, Jinan 250022, *China*

(Received 13 October 2025; revised manuscript received 3 January 2026; accepted manuscript online 23 January 2026)

While magnetic skyrmions in perpendicular magnetic anisotropy (PMA) systems are extensively studied, their realization in in-plane magnetic anisotropy (IMA) materials remains largely unexplored. Here, we demonstrate that Janus NbXTe (X = Se, S) monolayers host spontaneous tilted chiral textures, stabilized by substantial Dzyaloshinskii–Moriya interaction (DMI) (0.80 meV for NbSeTe, 0.59 meV for NbSTe) and intrinsic IMA. Combining first-principles calculations and atomistic spin dynamics simulations, we establish that perpendicular fields and biaxial strain independently reshape the energy landscape by tuning the competition among exchange, DMI, and anisotropy. Remarkably, while both materials spontaneously host skyrmions at zero field, NbSTe exhibits a superior field response, enabling multi-skyrmion nucleation at $\sim$ 0.2 T compared to $\sim$ 0.8 T for NbSeTe. Moreover, NbSTe sustains stability under 6% tensile strain, whereas NbSeTe undergoes topological degradation into chain-like textures. This work elucidates the stabilization mechanisms in two-dimensional (2D) IMA systems and identifies NbSTe as a robust candidate for low-power spintronic applications.

Keywords: skyrmions, Janus monolayers, strain engineering, Dzyaloshinskii–Moriya interaction

PACS: 75.70.Kw, 75.70.Ak, 75.30.Et, 71.15.Mb

DOI: 10.1088/1674-1056/ae3c8a **CSTR:** 32038.14.CPB.ae3c8a

1. Introduction

Magnetic skyrmions, nanoscale swirling spin textures characterized by non-trivial topological protection, have emerged as promising candidates for next-generation spintronic applications,[1–7] due to their ultralow driving current densities, enhanced stability, and potential for high-density information storage.[8–10] These topologically protected magnetic structures arise from the delicate interplay among various magnetic interactions,[11–14] with the Dzyaloshinskii–Moriya interaction (DMI) playing a pivotal role in their stabilization. To date, the majority of skyrmion research has focused on materials with perpendicular magnetic anisotropy (PMA), where skyrmions manifest as topological solitons aligned perpendicular to the material plane.[15,16] In such systems, the competition among ferromagnetic exchange, DMI, and magnetic anisotropy, often modulated by external magnetic fields, governs the stability and size of skyrmions.[17–19] Experimental observations have confirmed the existence of skyrmions in PMA materials, including magnetic multilayers,[20–22] bulk crystals,[23,24] and, more recently, two-dimensional van der Waals materials.[25,26] Parallel to these developments, significant progress has been achieved in related topological phases, such as the quantum anomalous Hall effect and the valley Hall effect in two-dimensional (2D) magnetic systems.[27–29]

It is known that materials with in-plane magnetic anisotropy (IMA) harbor equally rich magnetic texture diversity compared to PMA systems, yet remain significantly underexplored in the context of topological magnetism. In IMA systems, the magnetic easy axis lies within the material plane, fundamentally altering the energy landscape and enabling the formation of novel magnetic configurations.[30,31] The interplay between DMI and IMA can give rise to unconventional spin textures, including tilted skyrmions and helical structures, which exhibit distinct topological properties and dynamic behaviors.[32–35]

The 2D Janus materials, distinguished by intrinsic structural asymmetry, have recently garnered considerable attention as promising platforms for exhibiting substantial DMI and novel optoelectronic properties.[36–40] The broken inversion symmetry inherent in Janus structures naturally satisfies the crystallographic requirements for DMI,[41,42] while their reduced dimensionality enhances quantum confinement effects and spin–orbit coupling (SOC).[43,44] Among various Janus candidates, transition metal dichalcogenide (TMD) monolayers have shown particular promise due to their tunable magnetic properties and compatibility with existing device architectures.[45–47] Recent theoretical studies have suggested that Janus NbXTe (X = Se, S) monolayers possess favorable electronic and magnetic properties for hosting complex spin textures.[48–50] Moreover, strain engineering has been demonstrated to be an effective approach for manipulating chiral magnetic structures in similar Janus systems, such as the MnSeTe monolayer.[51] These materials combine the structural advantages of Janus compounds with the magnetic versatility of niobium-based systems,[52,53] potentially offering a unique platform for exploring IMA-driven topological

†Corresponding author. E-mail: ss_zhangchw@ujn.edu.cn

© 2026 Chinese Physical Society and IOP Publishing Ltd. All rights, including for text and data mining, AI training, and similar technologies, are reserved.

magnetism. However, a comprehensive investigation of their magnetic texture formation and the mechanisms for external control remains lacking.

In this work, we present a systematic first-principles investigation of tilted chiral magnetic textures in Janus NbXTe (X = Se, S) monolayers. By combining density functional theory calculations with atomistic spin dynamics simulations, we demonstrate that these materials intrinsically host spontaneous tilted magnetic textures driven by the interplay between substantial DMI and intrinsic IMA. Furthermore, we elucidate the tunability of these textures under external magnetic fields and mechanical strain, identifying optimal conditions for stabilizing isolated tilted skyrmions. Our findings not only advance the fundamental understanding of topological magnetism in IMA systems but also provide a theoretical framework for experimental realization and device applications.

2. Computational methods

All structural optimizations, electronic structure calculations, and magnetic parameter determinations were performed using the Vienna *ab initio* simulation package (VASP), which implements density functional theory (DFT). The exchange-correlation interactions were described using the Perdew–Burke–Ernzerhof (PBE) functional within the generalized gradient approximation (GGA). To account for the strong correlation effects of Nb 4d electrons, the DFT + U method was employed, with an effective Hubbard parameter $U_{\rm eff}$ set to 2.1 eV. The 2D Janus NbXTe (X = Se, S) monolayers were modeled using a slab geometry with a 17 Å vacuum layer to suppress spurious interlayer interactions. The crystal structures were fully relaxed until the residual forces on all atoms were less than 10^{-3} eV/Å, with an electronic energy convergence criterion of 10^{-6} eV. A plane-wave cutoff energy of 500 eV was employed throughout all calculations. The Brillouin zone was sampled using a Γ-centered $12\times12\times1$ k-point mesh. Additionally, the dynamical stability of the optimized structures was verified through phonon dispersion calculations using the PHONOPY code.

To investigate the magnetic properties of NbXTe monolayers, we employed the following spin Hamiltonian:

$$H = -J\sum_{\langle i,j\rangle} S_iS_j + K\sum_i (S_i^z)^2 - \sum_{\langle i,j\rangle} D_{ij}\cdot(S_i\times S_j) - \mu_{\rm Nb}B\sum_i S_i^z. \quad (1)$$

Here, S_i denotes the unit spin vector at the i-th Nb site, and $\langle i,j\rangle$ represents nearest-neighbor Nb pairs. The parameters J, K, and D_{ij} correspond to the Heisenberg exchange interaction, single-ion magnetic anisotropy, and DMI, respectively. The final term represents the Zeeman interaction, where $\mu_{\rm Nb}$ and B denote the atomic magnetic moment and the external magnetic field, respectively. The sign conventions are defined as follows: $J>0$ indicates ferromagnetic coupling, $K>0$ favors IMA, and the in-plane DMI component $d_\parallel>0$ favors clockwise (CW) spin rotation. Although itinerant electrons may mediate long-range interactions (e.g., RKKY) in metallic systems, we adopt the nearest-neighbor approximation, as direct exchange interaction dominates the energy scale. This minimal model sufficiently captures the essential physics of DMI-induced skyrmion formation, consistent with previous theoretical studies.[41,54–56]

To quantitatively determine the key magnetic parameters (J, K, $d_\parallel$), we performed energy mapping analysis based on DFT total energies. The nearest-neighbor Heisenberg exchange coupling J was derived from the energy difference between ferromagnetic (FM) and zigzag antiferromagnetic (AFM) configurations in a rectangular supercell. The exchange constant can be expressed as

$$J = \frac{E_{\rm AFM}-E_{\rm FM}}{8S^2}, \quad (2)$$

where $E_{\rm FM}$ and $E_{\rm AFM}$ represent the total energies of the FM and AFM configurations, respectively, and S denotes the magnitude of the unit spin vector ($|S|=1$).

The single-ion magnetic anisotropy K was determined from the energy difference between out-of-plane (z) and in-plane (x) spin orientations

$$K = \frac{E_z-E_x}{S^2}, \quad (3)$$

where E_z and E_x are the total energies with magnetization perpendicular and parallel to the monolayer plane, respectively. A positive K value indicates that the easy axis lies within the plane.

Then, the DMI strength $d_\parallel$ is evaluated using the energy difference between cycloidal spin spirals with opposite chiralities. The DMI parameter can be obtained as

$$d_\parallel = \frac{E_{\rm CW}-E_{\rm ACW}}{12S^2}, \quad (4)$$

where $E_{\rm CW}$ and $E_{\rm ACW}$ are the total energies of clockwise and anticlockwise spin configurations, respectively, and the factor 12 is derived from lattice geometry and the number of DMI-active bonds in the supercell.

Atomistic spin dynamics simulations were performed using the SPIRIT code on a $100\times100\times1$ two-dimensional lattice to investigate magnetic textures and their evolution under external perturbations.[57] Each lattice site represents an atomic magnetic moment with grid spacing equal to the material's lattice constant, and periodic boundary conditions were applied to simulate an effectively infinite monolayer. The simulations were conducted at $T\approx0$ K, utilizing the key magnetic parameters — including the nearest-neighbor exchange coupling strength, the DMI strength, and the magnetic anisotropy constant — extracted from our first-principles calculations. The temporal evolution of the spin unit vector $\boldsymbol{S}_i$ at site i is

governed by the Landau–Lifshitz–Gilbert (LLG) equation, expressed as

$$\frac{\partial \boldsymbol{S}_i}{\partial t} = -\frac{\gamma}{1+\alpha^2}\boldsymbol{S}_i \times \boldsymbol{H}_i^{\text{eff}} - \frac{\gamma\alpha}{1+\alpha^2}\boldsymbol{S}_i \times (\boldsymbol{S}_i \times \boldsymbol{H}_i^{\text{eff}}). \quad (5)$$

Here, γ is the gyromagnetic ratio, and α is the dimensionless Gilbert damping parameter. The effective magnetic field $\boldsymbol{H}_i^{\text{eff}}$ is defined as the negative functional derivative of the spin Hamiltonian (Eq. (1)) with respect to the local magnetic moment $\boldsymbol{m}_i = \mu_{\text{Nb}}\boldsymbol{S}_i$ (i.e., $\boldsymbol{H}_i^{\text{eff}} = -\frac{\partial \mathcal{H}}{\partial \boldsymbol{m}_i}$).

3. Results and discussion

Structural optimizations were performed for two-dimensional NbXTe (X = Se, S) monolayers to identify their ground-state configurations (Fig. 1). In these structures, the central Nb layer is asymmetrically sandwiched between two distinct chalcogen layers (Se/S and Te). This intrinsic out-of-plane asymmetry breaks inversion symmetry, establishing the structural foundation for DMI and enabling chiral magnetic texture formation. Symmetry analysis indicates that Janus NbXTe monolayers adopt a hexagonal structure with C_{3v} point group symmetry (space group $P3m1$). The calculated equilibrium lattice constants are 3.630 Å for NbSeTe and 3.561 Å for NbSTe, reflecting the smaller ionic radius of S compared to Se.

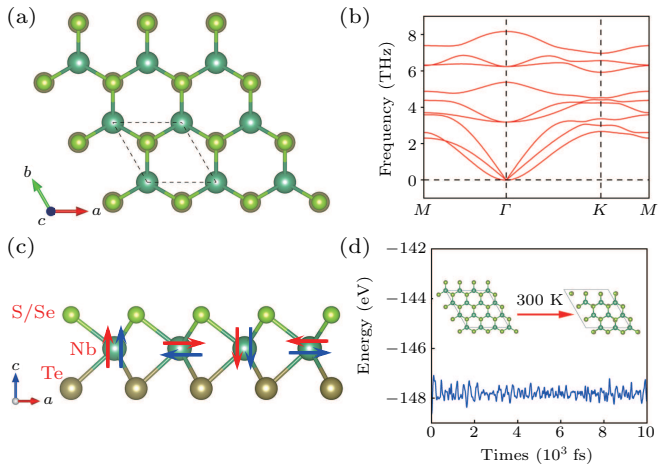


Fig. 1. (a) Top view of the Janus NbXTe (X = Se, S) monolayer structure. (b) Phonon dispersion spectrum of NbSeTe. (c) Side view of the monolayer; the superimposed arrows indicate the two spin configurations with opposite chiralities used to calculate DMI parameters. (d) Variations of the total energy during *ab initio* molecular dynamics (AIMD) simulations for NbSeTe at 300 K.

To evaluate the structural stability, we performed phonon dispersion calculations and AIMD simulations. As shown in Fig. 1(b), the phonon dispersion of the NbSeTe monolayer exhibits no imaginary modes throughout the Brillouin zone, confirming dynamical stability. Furthermore, 10 ps AIMD simulations at 300 K were conducted to assess thermal stability. The total energy remains stable with minimal fluctuations around the equilibrium value (Fig. 1(d)), and the atomic configuration preserves its structural integrity without significant distortion. These results confirm that Janus NbXTe monolayers are dynamically and thermally stable, providing a solid foundation for investigating their magnetic properties and potential topological spin textures.

To investigate the magnetic properties, we calculated the exchange coupling parameters for Janus NbSeTe and NbSTe monolayers, as shown in Fig. 2(a). The NbSeTe monolayer exhibits stronger exchange interactions (J) than NbSTe, consistent with its higher Curie temperature ($T_C \approx 148$ K vs. 69 K for NbSTe) obtained from Monte Carlo simulations (Fig. 3(a)). Both monolayers display pronounced IMA ($K > 0$) of approximately 3.6 meV, which favors the formation of tilted skyrmions rather than the perpendicular skyrmions typical of systems with PMA. The calculated DMI strengths are $d_{\parallel} = 0.802$ meV for NbSeTe and $d_{\parallel} = 0.592$ meV for NbSTe. These substantial DMI values, arising from the interplay between spin–orbit coupling and the broken inversion symmetry inherent to the Janus structure, indicate favorable conditions for stabilizing chiral magnetic textures.

To elucidate the atomic origins of DMI, we analyzed the SOC energy differences corresponding to opposite chiralities, as presented in Fig. 2(b). Similar to DMI mechanisms in ferromagnet/heavy metal heterostructures (Fert–Levy type), the interaction primarily stems from heavy metal contributions. For NbSTe, Nb and Te atoms provide the dominant contributions, while S atoms contribute minimally. This reflects the strong SOC of Te atoms and their interaction with neighboring Nb atoms. In NbSeTe, Te atoms contribute most significantly, followed by Nb atoms, with Se atoms contributing least. This enhancement in Te contributions upon S → Se substitution reflects changes in the local atomic environment, SOC strength, and orbital hybridization patterns.

Figure 2(c) further displays the ELF distribution along the [110] direction for NbSeTe. The high ELF regions clearly delineate covalent bonds between Nb and chalcogen atoms. Crucially, the Janus structure creates pronounced asymmetry in the ELF distribution between Nb–Se and Nb–Te bonds. The Nb–Te bond exhibits stronger electron localization and distinct spatial morphology compared to the Nb–Se bond, directly manifesting the broken inversion symmetry at the electronic level. This microscopic asymmetry, coupled with SOC, provides the fundamental physical basis for DMI generation.

The magnetic transition temperature (T_C) is a critical parameter for evaluating the thermal stability of magnetic order. We determined T_C for NbSeTe and NbSTe monolayers via Monte Carlo (MC) simulations using the mcsolver package.[58] As shown in Fig. 3, T_C was identified from the peak in the temperature-dependent specific heat capacity (C_v), which marks the magnetic phase transition. The estimated values are $T_C \approx 148$ K for NbSeTe and 69 K for NbSTe. The substantially higher T_C of NbSeTe correlates directly with its

stronger exchange coupling, confirming that enhanced magnetic interactions stabilize magnetic ordering at higher temperatures.

To explore their potential for two-dimensional spintronic applications, we further investigated the effects of biaxial strain on magnetic ground-state stability, focusing on the evolution of chiral magnetic textures. Our analysis ranges from −2% (compressive) to +6% (tensile) strain, covering the experimentally accessible range for mechanical tuning of 2D materials.

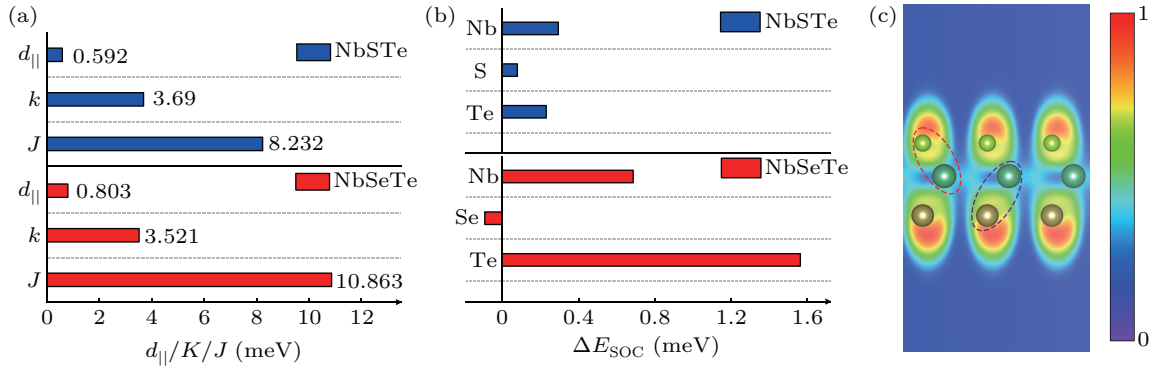


Fig. 2. (a) Exchange coupling strength (J), DMI strength ($d_{||}$), and magnetic anisotropy constant (K) for NbSeTe and NbSTe monolayers. (b) Atom-resolved localization of the SOC energy difference (ΔE_{SOC}) originating from different atomic types. (c) Electron localization function (ELF) map of the NbSeTe monolayer.

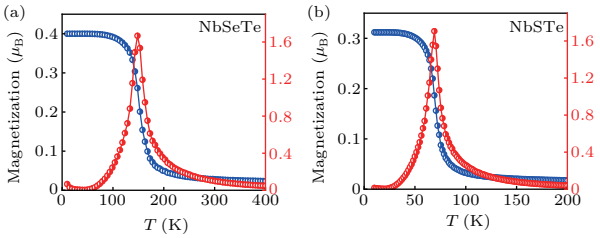


Fig. 3. Monte Carlo simulations of magnetization (blue) and specific heat (red) for (a) NbSeTe and (b) NbSTe monolayers.

To elucidate how biaxial strain modifies the magnetic properties of NbXTe monolayers, we first evaluated the stability of the magnetic ground state and the evolution of key interaction parameters. As shown in Figs. 4(a) and 4(d), energy differences between FM and AFM configurations indicate that the FM state remains the ground state across the entire strain range investigated (−2% to +6%). This robust ferromagnetic ordering under mechanical deformation provides a stable foundation for tuning chiral magnetic textures. The strain dependence of the nearest-neighbor exchange coupling (J), however, exhibits distinct behavior in the two materials. For NbSeTe (Fig. 4(b)), J increases monotonically with tensile strain, from approximately 9.6 meV to 15.1 meV — a trend attributed to the modulation of orbital overlap by increased interatomic distances, which strengthens the exchange interaction. In contrast, NbSTe (Fig. 4(e)) displays non-monotonic behavior: J initially increases under tension, reaches a maximum of approximately 8.3 meV at 1%–2% strain, and subsequently decreases. This distinct trend likely originates from a complex interplay between strain-induced changes in Nb–S bond geometry and orbital hybridization, where optimal conditions for exchange coupling occur at intermediate strain levels.

Next, we analyzed the effect of strain on the magnetic anisotropy constant (K), which is crucial for stabilizing tilted spin textures. As shown in Figs. 4(c) and 4(f), both materials exhibit a monotonic reduction in K with increasing tensile strain, indicating a weakening of intrinsic IMA. However, their sensitivities to strain differ markedly. NbSeTe shows a moderate decrease, with K declining from $\sim$ 4.0 meV at −2% strain to $\sim$ 2.05 meV at +6% strain. NbSTe, in contrast, displays a far more pronounced response: K decreases from $\sim$ 4.25 meV to $\sim$ 0.7 meV over the same range. This substantial softening of the easy-plane character in NbSTe under tensile strain is particularly noteworthy, as it dramatically lowers the energy penalty for out-of-plane spin canting. The divergent strain responses of exchange coupling and magnetic anisotropy in NbSeTe and NbSTe highlight the material-specific tunability of their magnetic energy landscapes. The ability to precisely weaken IMA — especially in NbSTe — while maintaining robust ferromagnetism is critical for engineering tilted skyrmions. This interplay between strain-modified anisotropy and DMI provides a powerful mechanism for controlling the stability and morphology of such chiral textures, as explored further below.

Having established the strain-tunable nature of exchange coupling and anisotropy, we now turn to the DMI, a key ingredient for chiral magnetism. As illustrated in Figs. 5(a) and 5(c), both NbXTe monolayers exhibit pronounced, non-monotonic variation in DMI strength $d_{||}$ under biaxial strain, revealing a complex yet powerful control mechanism. For NbSeTe, $d_{||}$ varies around its zero-strain value of 0.80 meV, peaking at $\sim$ 0.86 meV under 2% compression and showing an initial decrease followed by recovery under tension. Similarly, NbSTe displays a non-trivial strain dependence: $d_{||}$ initially decreases under tension before rising to $\sim$ 0.61 meV at +6% strain.

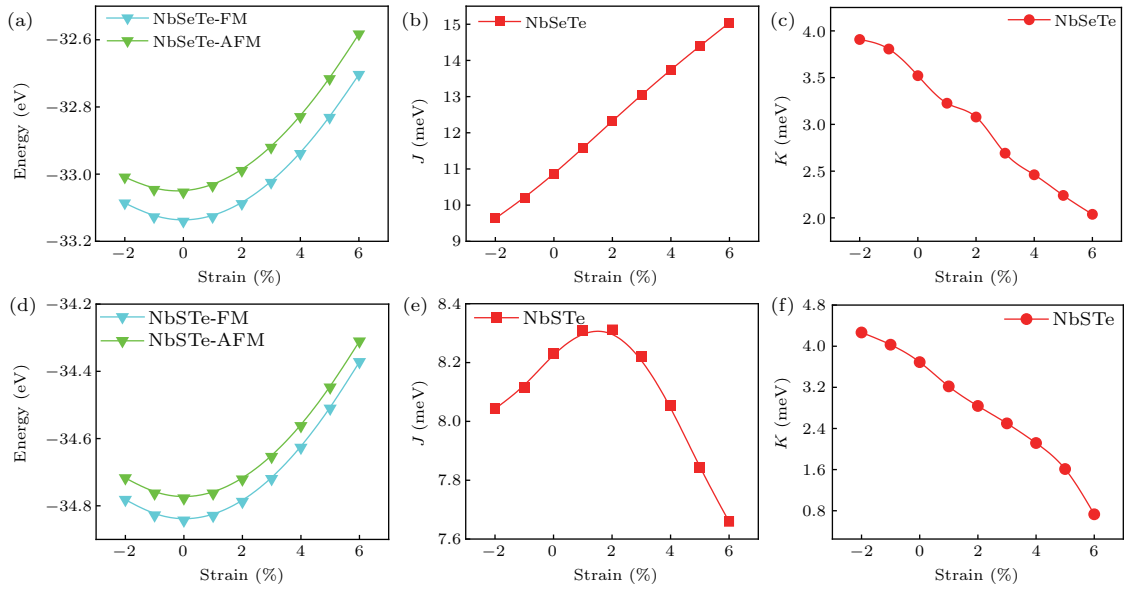


Fig. 4. Energies of (a) and (d) zigzag-AFM and FM ground-state configurations, (b) and (e) nearest-neighbor exchange coupling strength (J), and (c) and (f) magnetic anisotropy constant (K) for NbSeTe and NbSTe monolayers under different biaxial strains.

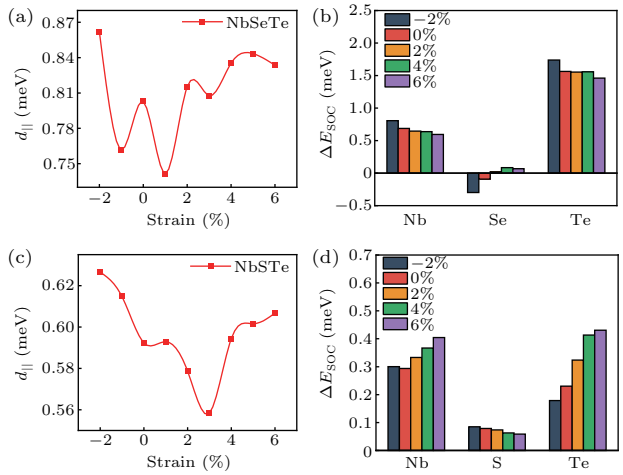


Fig. 5. Evolution of DMI properties under biaxial strain. (a) and (c) variations of the total DMI strength ($d_{\parallel}$), and (b) and (d) atom-resolved localization of the SOC energy difference (ΔE_{SOC}) originating from Nb, Se/S, and Te atoms.

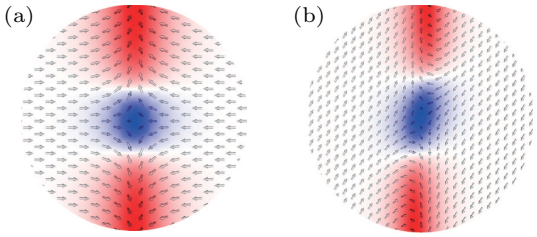


Fig. 6. Initial magnetic textures of NbSeTe and NbSTe monolayers in their intrinsic states: (a) NbSeTe, (b) NbSTe.

To understand the microscopic origins of this behavior, we decomposed the DMI into atom-resolved contributions by analyzing SOC energy differences, as shown in Figs. 5(b) and 5(d). In NbSeTe, the overall non-monotonic trend arises from competing atomic contributions. While Te atoms, driven by their strong SOC, provide the dominant positive contribution across all strains, both their influence and that of Nb atoms gradually diminish with increasing tensile strain. Concurrently, the Se contribution undergoes a sign reversal, transitioning from negative under compression to positive under tension. This interplay of diminishing positive contributions and a sign-changing term leads to the observed fluctuation in the total DMI. In contrast, the mechanism in NbSTe is more straightforward: contributions from both Nb and Te atoms increase monotonically with tensile strain, while the S contribution steadily decreases. This redistribution of atomic influence is key — at higher tensile strains, the rapidly strengthening positive contributions from Nb and especially Te atoms effectively outweigh the weakening negative contribution from S, driving the overall DMI recovery and enhancement. This analysis reveals that macroscopic DMI tunability is governed by a delicate, strain-dependent balance of competing atomic-level interactions.

Furthermore, atomistic spin dynamics (ASD) simulations were performed for both NbXTe monolayers under periodic boundary conditions in the absence of external fields or strain. As illustrated in Fig. 6, the resulting spin configurations exhibit tilted chiral textures with skyrmion-like morphology. Specifically, NbSeTe forms a highly symmetric tilted skyrmion with a well-defined circular core (Fig. 6(a)), whereas NbSTe (Fig. 6(b)) displays a noticeably more distorted texture, featuring an irregularly shaped core and pronounced anisotropic spin distribution. These spontaneous non-collinear structures originate from energetic competition between IMA, which favors in-plane spin alignment, and DMI, which drives chirality and spin canting. The distinct morphologies directly reflect the material-specific interplay of intrinsic magnetic parameters in each system.

In addition, the effects of a perpendicular magnetic field (B_z) on the magnetic texture reveal distinct field-dependent

evolution pathways. The NbSeTe monolayer exhibits a systematic evolution with increasing field strength (Figs. 7(a)–7(f)). At zero field, the system spontaneously forms tilted textures through the competition between IMA and DMI, manifesting as parallel domain walls with opposite chirality under periodic boundary conditions. These walls contain tilted, continuously rotating magnetic moments. Under weak fields (Fig. 7(c), 0.8 T), the Zeeman effect reconstructs the domain wall structure into parallel domains containing two isolated skyrmion-like cores. This two-skyrmion configuration persists at intermediate fields (Figs. 7(d)–7(e), 1.2–2.0 T) as the enhanced Zeeman coupling strengthens the out-of-plane components. Finally, at high fields (Fig. 7(f), 5.0 T), the Zeeman energy dominates, overcoming any structural barriers to achieve uniform ferromagnetic saturation.

In comparison, NbSTe displays a similar overall evolution but with a significantly accelerated low-field response. At a relatively low field of 0.2 T (Fig. 7(h)), the system already forms two distinct, isolated skyrmion cores, indicating a lower energy threshold for skyrmion formation compared to NbSeTe. This enhanced sensitivity reflects the specific magnetic parameter ratios in NbSTe, where the energy balance favoring skyrmion stability is achieved at a much-reduced field strength. Furthermore, while both materials eventually reach saturation, NbSTe exhibits enhanced skyrmion stability at higher fields. These distinct behaviors underscore the tunability of magnetic textures through both material engineering and external field control.

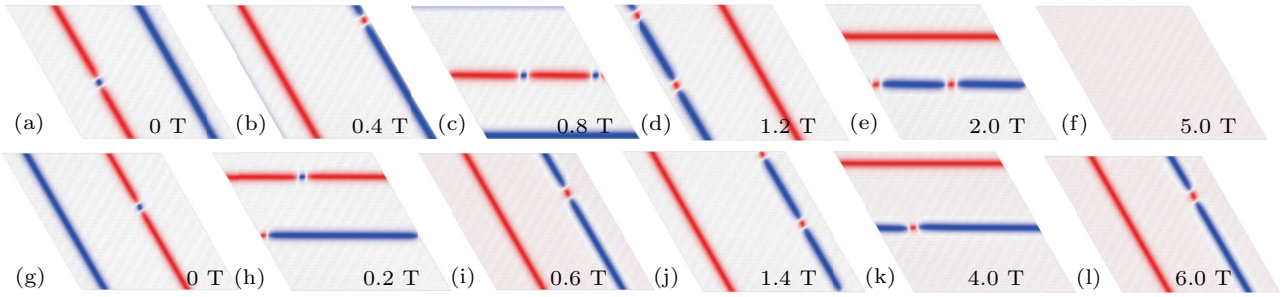


Fig. 7. Simulation results under different magnetic fields: (a)–(f) NbSeTe, (g)–(l) NbSTe.

Figure 8 further demonstrates the modulation of magnetic textures by biaxial strain in 2D NbSeTe and NbSTe monolayers. Under a -2% compressive strain, the complex chiral textures in both materials are significantly simplified, with their intrinsic skyrmion cores suppressed. This transformation results in chain-like arrangements of domains separated by tilted domain walls. Such structural changes indicate that compressive strain fundamentally alters the energetic balance among the underlying magnetic interactions. Specifically, it enhances contributions favoring collinear spin alignment, causing these fragmented, chain-like configurations to become the new ground state.

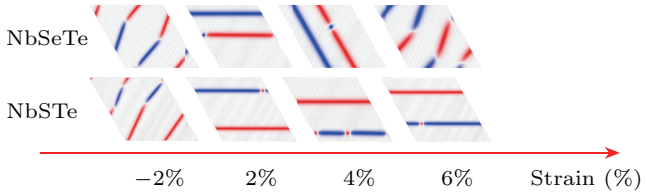


Fig. 8. Simulation results under different strains.

The two materials exhibit markedly different responses under tensile strain, although both are capable of forming skyrmion cores. In NbSeTe, increasing tensile strain causes the skyrmion-like domains to progressively widen, eventually transitioning into a multi-segmented chain structure at higher strains — morphologically similar to the compressive case. This evolution is attributed to the strain-induced increase in exchange coupling and a concurrent decrease in easy-plane anisotropy. While a skyrmion core can initially form, the dominant increase in J and decrease in K eventually overwhelm the stabilizing influence of $d_{\parallel}$, rendering the extended chain structure more energetically favorable than isolated skyrmions. In stark contrast, NbSTe demonstrates an enhanced capability to both form and sustain skyrmions. It nucleates two distinct skyrmion cores at 4% tensile strain and, remarkably, retains a stable skyrmion core even at larger strains. This behavior is highly consistent with our magnetic field-tuning results, confirming that NbSTe possesses an intrinsic propensity for forming more stable and robust skyrmions.

4. Conclusion

In summary, this study systematically elucidates the formation mechanisms of tilted chiral magnetic structures in Janus NbSeTe and NbSTe monolayers through combined first-principles calculations and atomistic spin dynamics simulations. We establish that intrinsic in-plane magnetic anisotropy and substantial Dzyaloshinskii–Moriya interaction are essential for stabilizing these non-collinear topological states, with both monolayers spontaneously hosting tilted chiral textures at zero field. Despite similar ground-state configurations, the two materials exhibit markedly different tunability: NbSeTe requires relatively high fields (~ 0.8 T) for efficient multi-skyrmion nucleation, and its topological order degrades into

chain-like textures under larger tensile strains, whereas NbSTe emerges as a superior platform, enabling multi-skyrmion nucleation at remarkably low fields (~ 0.2 T) while preserving topological order under tensile strains up to 6%. This contrast arises from distinct competition among exchange, DMI, and anisotropy, which reshapes the energy landscape under external perturbations. Our findings highlight the dominant role of intrinsic material properties in determining the efficacy of external control, positioning NbSTe as a promising candidate for low-power spintronic applications and motivating future experimental validation of chiral magnetic states in 2D IMA systems.

Acknowledgment

Project supported by the Natural Science Foundation of Shandong Province, China (Grant No. SZR2536).

References

[1] Skyrme T H R 1962 *Nucl. Phys.* **31** 556
[2] Rossler U K, Bogdanov A N and Pfleiderer C 2006 *Nature* **442** 797
[3] Han J H, Zang J D, Yang Z H, Park J H and Nagaosa N 2010 *Phys. Rev. B* **82** 184403
[4] Wang Y P, Ji W X, Zhang C W, Li P, Zhang S F, Wang P J, Li S S and Yan S S 2017 *Appl. Phys. Lett.* **110** 213101
[5] Zhang S J, Zhang C W, Zhang S F, Ji W X, Li P, Wang P J, Li S S and Yan S S 2017 *Phys. Rev. B* **96** 205433
[6] Zhang M H, Zhang C W, Wang P J and Li S S 2018 *Nanoscale* **10** 20226
[7] Li S S, Ji W X, Hu S J, Zhang C W and Yan S S 2017 *ACS Appl. Mater. Interfaces* **9** 41443
[8] Jonietz F, Muhlbauer S, Pfleiderer C, Neubauer A, Munzer W, Bauer A, Adams T, Georgii R, Boni P, Duine R A, Everschor K, Garst M and Rosch A 2010 *Science* **330** 1648
[9] Fert A, Cros V and Sampaio J 2013 *Nat. Nanotechnol.* **8** 152
[10] Tomasello R, Martinez E, Zivieri R, Torres L, Carpentieri M and Finocchio G 2014 *Sci. Rep.* **4** 6784
[11] Nagaosa N and Tokura Y 2013 *Nat. Nanotechnol.* **8** 899
[12] Dzyaloshinsky I 1958 *J. Phys. Chem. Solids* **4** 241
[13] Bogdanov A and Hubert A 1994 *J. Magn. Magn. Mater.* **138** 255
[14] Moriya T 1960 *Phys. Rev.* **120** 91
[15] Woo S, Litzius K, Kruger B, Im M Y, Caretta L, Richter K, Mann M, Krone A, Reeve R M, Weigand M, Agrawal P, Lemesh I, Mawass M A, Fischer P, Klaui M and Beach G S D 2016 *Nat. Mater.* **15** 501
[16] Soumyanarayanan A, Raju M, Gonzalez Oyarce A L, Tan A K C, Im M Y, Petrovic A P, Ho P, Khoo K H, Tran M, Gan C K, Ernult F and Panagopoulos C 2017 *Nat. Mater.* **16** 898
[17] Zhang X C, Zhou Y, Song K M, Park T E, Xia J, Ezawa M, Liu X, Zhao W S, Zhao G P and Woo S 2020 *J. Phys. Condens. Matter* **32** 143001
[18] Everschor-Sitte K, Masell J, Reeve R M and Klaui M 2018 *J. Appl. Phys.* **124** 240901
[19] Jiang W, Chen G, Liu K, Zang J D, te Velthuis S G E and Hoffmann A 2017 *Phys. Rep.* **704** 1
[20] Boulle O, Vogel J, Yang H X, Pizzini S, de Souza Chaves D, Locatelli A, Mentes T O, Sala A, Buda-Prejbeanu L D, Klein O, Belmeguenai M, Roussigne Y, Stashkevich A, Cherif S M, Aballe L, Foerster M, Chshiev M, Auffret S, Miron I M and Gaudin G 2016 *Nat. Nanotechnol.* **11** 449
[21] Legrand W, Maccariello D, Ajejas F, Collin S, Vecchiola A, Bouzehouane K, Reyren N, Cros V and Fert A 2019 *Nat. Mater.* **19** 34
[22] Zeissler K, Finizio S, Shahbazi K, Massey J, Ma'Mari F A, Bracher D M, Kleibert A, Rosamond M C, Linfield E H, Moore T A, Raabe J, Burnell G and Marrows C H 2018 *Nat. Nanotechnol.* **13** 1161
[23] Yu X Z, Koshibae W, Tokunaga Y, Shibata K, Taguchi Y, Nagaosa N and Tokura Y 2018 *Nature* **564** 95
[24] Karube K, White J S, Reynolds N, Gavilano J L, Oike H, Kikkawa A, Kagawa F, Tokunaga Y, Ronnow H M, Tokura Y and Taguchi Y 2016 *Nat. Mater.* **15** 1237
[25] Zhang Y, Xu C S, Chen P, Nahas Y, Prokhorenko S and Bellaiche L 2020 *Phys. Rev. B* **102** 054435
[26] Ding B, Li Z F, Xu G Z, Li H, Hou Z P, Liu E K, Xi X K, Xu F, Yao Y and Wang W H 2020 *Nano Lett.* **20** 868
[27] Wang M L, Li S S, Wang Y P, Dong X J, Li F, Ji W X and Zhang C W 2025 *Phys. Rev. B* **112** 174414
[28] Wu B, Song Y L, Ji W X, Wang P J, Zhang S F and Zhang C W 2023 *Phys. Rev. B* **107** 214419
[29] Sun H, Li S S, Ji W X and Zhang C W 2022 *Phys. Rev. B* **105** 195112
[30] Shen L, Xia J, Zhang X C, Ezawa M, Tretiakov O A, Liu X, Zhao G P and Zhou Y 2020 *Phys. Rev. Lett.* **124** 157202
[31] Goebel B, Mertig I and Tretiakov O A 2021 *Phys. Rep.* **895** 1
[32] Zhang S L, Wang W W, Burn D M, Peng H, Berger H, Bauer A, Pfleiderer C, van der Laan G and Hesjedal T 2018 *Nat. Commun.* **9** 2115
[33] Jin C L, Wang J B, Wang W, Song C L, Wang J F, Xia H L and Liu Q F 2018 *Phys. Rev. Appl.* **9** 044007
[34] Hoffmann M, Zimmermann B, Muller G P, Schurhoff D, Kiselev N S, Melcher C and Blugel S 2017 *Nat. Commun.* **8** 308
[35] Rybakov F N, Borisov A B, Blugel S and Kiselev N S 2016 *New J. Phys.* **18** 045002
[36] Lu A Y, Zhu H, Xiao J, Chuu C P, Han Y, Chiu M H, Cheng C C, Yang C W, Wei K H, Yang Y, Wang Y, Sokaras D, Nordlund D, Yang P, Muller D A, Chou M Y, Zhang X and Li L J 2017 *Nat. Nanotechnol.* **12** 744
[37] Zhang J, Jia S, Kholmanov I, Dong L, Er D, Chen W B, Guo H, Jin Z H, Shenoy V B, Shi L and Lou J 2017 *ACS Nano* **11** 8192
[38] Dong L, Lou J and Shenoy V B 2017 *ACS Nano* **11** 8242
[39] Chen M, Yu S B, Zhang D and Li J 2023 *Chin. Phys. Lett.* **40** 087201
[40] Qi Y X, Zhao J and Zeng H 2024 *Chin. Phys. B* **33** 096302
[41] Yuan J R, Yang Y M, Cai Y Q, Wu Y H, Chen Y P, Yan X H and Shen L 2020 *Phys. Rev. B* **101** 094420
[42] Tong Q J, Liu F, Xiao J and Yao W 2018 *Nano Lett.* **18** 7194
[43] Xiao D, Liu G B, Feng W X, Xu X D and Yao W 2012 *Phys. Rev. Lett.* **108** 196802
[44] Yao W, Xiao D and Niu Q 2008 *Phys. Rev. B* **77** 235406
[45] Hu T, Jia F H, Zhao G D, Wu J C, Stroppa A and Ren W 2018 *Phys. Rev. B* **97** 235404
[46] Chaurasiya R and Dixit A 2019 *Appl. Surf. Sci.* **490** 204
[47] Yagmurcukardes M, Qin Y, Ozen S, Sayyad M, Peeters F M, Tongay S and Sahin H 2020 *Appl. Phys. Rev.* **7** 011311
[48] Guo Y D, Zhang Y, Yuan S M, Wang B and Wang J J 2018 *Nanoscale* **10** 18036
[49] Torun E, Sahin H, Cahangirov S, Rubio A and Peeters F M 2016 *J. Appl. Phys.* **119** 074307
[50] Wu Y L, Zeng Z Y, Geng H Y and Chen X R 2024 *J. Appl. Phys.* **136** 093904
[51] Wang Z W, Liang J H and Yang H X 2023 *Chin. Phys. Lett.* **40** 017501
[52] Zhao Y H, Lin L F, Zhou Q H, Li Y H, Yuan S J, Chen Q, Dong S and Wang J L 2018 *Nano Lett.* **18** 2943
[53] Webster L and Yan J A 2018 *Phys. Rev. B* **98** 144411
[54] Han P, Zhang J T, Shi S B, Wang Z H, Xu T and Wang J 2025 *Appl. Phys. Lett.* **127** 102406
[55] Han Y T, Ji W X, Wang P J, Li P and Zhang C W 2023 *Nanoscale* **15** 6830
[56] Cui Q R, Liang J H, Shao Z J, Cui P and Yang H X 2020 *Phys. Rev. B* **102** 094425
[57] Muller G P, Hoffmann M, Disselkamp C, Schurhoff D, Mavros S, Sallermann M, Kiselev N S, Jonsson H and Blugel S 2019 *Phys. Rev. B* **99** 224414
[58] Liu L, Ren X, Xie J H, Cheng B, Liu W K, An T Y, Qin H W and Hu J F 2019 *Appl. Surf. Sci.* **480** 300